Köhl *et al. Geotherm Energy* (2020) 8:26
https://doi.org/10.1186/s40517-020-00180-x

Geothermal Energy

RESEARCH Open Access

Hydrochemical and operational parameters driving carbonate scale kinetics at geothermal facilities in the Bavarian Molasse Basin

Bernhard Köhl[1*], Martin Elsner[1] and Thomas Baumann[2]

*Correspondence:
bernhard.koehl@tum.de
[1] Chair of Analytical Chemistry and Water Chemistry, Technical University of Munich, Marchioninistrasse 17, 81377 München, Germany
Full list of author information is available at the end of the article
This publication is dedicated to the memory of our friend and colleague Dr. Achim Schubert.

Abstract

The majority of scales observed at geothermal facilities exploring the Malm Aquifer in the Bavarian Molasse Basin are carbonates. They form due to a disruption of the lime–carbonic acid equilibrium during production caused by a reduction of the partial pressure of carbon dioxide due to pressure change and degassing. These scales are found at the pumps, production pipes, filters, heat exchangers, and occasionally in the injection pipes. In this study, scales of all sections of geothermal facilities were taken. The database consists of scale samples from 13 geothermal pumps, 6,000 m production pipe (sample interval 10 - 12 m), 11 heat exchanger revisions, 2 injection pipes, and numerous filter elements. The samples were analyzed by SEM-EDX, XRD, Raman spectroscopy, and acid digestion to assess their chemical and mineralogical composition. From direct gauge measurements at six facilities during pump changes, scale rates were determined along the production pipes. From indirect measurements (multifinger caliper measurements) scale rates are derived for the region below the pump. Hydrochemical analyses from the wellhead were taken from 13 sites to feed the hydrogeochemical models. The calcite scale rates in the production pipes increase from the pump to the wellhead, where they reach 1.5 - 4.1 μmol/(m^2 · s). Scale rates below the pump reach up to 1.5 μmol/(m^2 · s). Given the slight change of hydrochemistry on the rise through the production pipe, where < 4 % of dissolved calcium ions precipitate as scale, scale rates cannot be derived from water samples at the wellhead, but require direct gauge measurements. The small amount of precipitation, together with fully turbulent conditions suggests that all measured rates are controlled by the surface-reaction of calcite crystallization following the nomenclature of Appelo and Postma (2004). Two approaches are used for the modeling of the scale rates. The first approach is based on hydrogeochemical modeling with PHREEQC. Scale rates calculated by this method are one order of magnitude higher than the measured ones. The second approach is based on correlations between the measured scale rates at the wellhead at six facilities and identified thermodynamic scale drivers (Δ log (pCO_2), Δ total pressure, Δ pH, and $SI_{calcite}$). The correlations allow linear regressions which are used for the prediction of the scale rate at the wellhead, along the whole production pipe, and below. The modeling results show that scale prediction based on the new regressions that rely on thermodynamic scale drivers works better than existing hydrogeochemical models,

already without implementation of kinetic parameters (CO_2-stripping and magnesium inhibition).

Keywords: Scales, Scaling, Precipitation, Rate, Kinetics, Calcite, $CaCO_3$, Carbonate, Malm aquifer, Bavarian Molasse Basin, PHREEQC, Modeling

Introduction

Geothermal energy usage in the Bavarian Molasse Basin

Geothermal energy is a promising part of a renewable energy mix providing green energy year round (Bayerisches Staatsministerium 2019). The carbonate sedimentary rocks of the Upper Jurassic, also called 'Malm aquifer', located in the Bavarian Molasse Basin (BMB), host a large potential for geothermal usage with temperatures of up to 150 °C and flow rates up to 150 L/s (Bauer et al. 2014; Eyerer et al. 2017). In 2018, 26 geothermal facilities with a total power of 296 MW_{th} and 34 MW_{el} were installed (Flechtner and Aubele 2019), and many new projects are planned or are already in construction Bayerisches Staatsministerium (2019). The local energy provider of Munich, the Stadtwerke München (SWM), is dedicated to the goal of providing the capital of Bavaria with 100 % carbon dioxide-neutral heat by the year 2040, mainly by further development of geothermal energy production from the Bavarian Malm aquifer (Stadtwerke München 2019).

The geothermal facilities producing from the Bavarian Malm aquifer are composed of doublet or triplet systems with one or two production wells, and one or two injection wells. By the use of an electrical submersible pump (ESP), hot geothermal water is pumped from a depth of up to 5,000 m to the surface. Here, the energy is transferred by heat exchangers to district heating systems or to a power generation unit (e.g. organic Rankine cycle—ORC). This way, only the heat of the thermal water is extracted, but the thermal water circulates in a closed system. After heat extraction, the cooled water is reinjected into the same aquifer through the injection well, which reaches the target aquifer typically in a few kilometers of horizontal distance (Bauer et al. 2014).

Mineral precipitation and buildup in pipes, also known as scales or scalings, are a common problem of geothermal plants. Growth of scale in pipes reduces the technical and economic efficiency of geothermal plants, and requires frequent, costly maintenance or even process modification of installed geothermal plants. Mineral buildup can occur on any surface exposed to the geothermal fluid, including the submersible pump, its motor, the production pipes, and ground-level components, such as heat exchangers (Wanner et al. 2017; Herbrich 2016; Boch et al. 2017).

Background of $CaCO_3$ scale formation

The thermal water contained in the aquifer has equilibrated with the carbonate rock during its long residence time according to the carbonic acid equilibrium (Wanner et al. 2017). This equilibrium is maintained by three parallel occurring reactions depending on pH and temperature (Equations 1 - 3) (Appelo and Postma 2004). When the pH rises or when CO_2 is removed from the system, the equilibrium shifts so that the solubility is exceeded, and dissolved calcium carbonate ($CaCO_3$) can precipitate.

$$CaCO_3 + H^+ \rightleftharpoons Ca^{2+} + HCO_3^-, \quad (1)$$

$$CaCO_3 + H_2CO_3^* \rightleftharpoons Ca^{2+} + 2HCO_3^-, \tag{2}$$

$$CaCO_3 + H_2O \rightleftharpoons Ca^{2+} + HCO_3^- + OH^-, \tag{3}$$

where $H_2CO_3^* = CO_{2_{(aq)}} + H_2CO_3$. At 25 °C only 0.2 % of $H_2CO_3^*$ is carbonic acid (H_2CO_3) while the major part is dissolved aqueous $CO_{2_{(aq)}}$ (Appelo and Postma 2004). The distribution of the carbonate species can be calculated by hydrochemical speciation software, e.g. the open-source software PHREEQC (Parkhurst and Appelo 1999). Note that for internal calculation, PHREEQC does not differentiate between $CO_{2_{(aq)}}$ and H_2CO_3, and summarizes these two species with the name of the more abundant species $CO_{2_{(aq)}}$ (Appelo and Postma 2004). To account for other species and complexes which are relevant in carbonate systems, PHREEQC, which uses the thermodynamic data from the database phreeqc.dat, also calculates the activities of $CO_{2_{(g)}}$, $CaHCO_3^+$, $CaOH^+$, $CaSO_4$, $MgCO_3$, and $MgHCO_3^+$.

The solubility product (Equation 4) for calcite at 25 °C is $3.3 \cdot 10^{-9}$ mol^2 / L^2, respectively, the $\log_K$ is -8.48 mol^2/ L^2 (Parkhurst and Appelo 1999). The solubility of calcite decreases strongly with increasing temperature.

$$K_{sp}(CaCO_3) = [Ca^{2+}] \cdot [CO_3^{2-}], \tag{4}$$

where K_{sp} is the solubility product, and $[Ca^{2+}]$ and $[CO_3^{2-}]$ are the activities of dissolved $[Ca^{2+}]$ and $[CO_3^{2-}]$ ions that can coexist in equilibrium with solid calcite.

The saturation index of calcite ($SI_{calcite}$) indicates if the solubility product is exceeded. In other words, the SI shows if the $CaCO_3$ resulting from Equations 1 – 3 stays dissolved ($SI_{calcite} \leq 0$) or precipitates ($SI_{calcite} > 0$).

The SI is defined as

$$SI = log \frac{IAP}{K_{sp}}, \tag{5}$$

where IAP is the ion activity product of the actual activities of Ca^{2+} and CO_3^{2-}, as explained in detail in Appelo and Postma (2004).

Due to the carbonatic matrix in the Malm aquifer, the geothermal fluid has a carbonatic composition, and 95 % of the observed scales consist of $CaCO_3$. Most of the $CaCO_3$ is calcite where a minor portion (6 - 7 mol %) of calcium is substituted by magnesium (Wanner et al. 2017; Herbrich 2016; Boch et al. 2017; Eichinger 2016).

For the calculation of $SI_{calcite}$, PHREEQC uses the ion activity product and solubility product according to Eqs. 4 and 5. For the calculation of the calcite precipitation kinetics, the rate equation of Plummer et al. (1978) is implemented in PHREEQC according to Equation 6. This equation combines Eqs. 1 – 3, and adds the backward reaction, i.e. precipitation. Further lab experiments determined rate constants based on this equation (Chou et al. 1989; Talman et al. 1990).

$$r = k_1 \cdot [H^+] + k_2 \cdot [H_2CO_3] + k_3 \cdot [H_2O] - k_4 \cdot [Ca^{2+}][HCO_3^-] \tag{6}$$

with the specific reaction rate r of dissolution, the rate constants k_1, k_2, k_3 and k_4, and the activities of the reactants. The first term of the equation depends on $[H^+]$, respectively

pH, and is important at pH < 3.5. The second term is dominant at a pH of 3.5 - 7.0, depends on $[H_2CO_3]$, and is controlled by partial pressure of CO_2. The third term has a major effect at pH > 7.0 and represents hydrolysis of $CaCO_3$. The fourth term describes the backwards reaction of the first term, i.e. precipitation. However, as long as $[H^+]$ and $[H_2CO_3]$ stay constant, the fourth term also accounts for the backward reaction of the second and third terms (Appelo and Postma 2004; Plummer et al. 1978).

These rate constants are dependent on temperature and activity coefficients. Diffusion is not incorporated in the equation, assuming fully mixed conditions. Since in field experiments mixture is not always complete, a diffusive boundary layer may form, leading to smaller rates than the theoretically calculated ones (Dreybrodt et al. 1992; Plummer et al. 2000).

The overall reaction rate for the dissolution/precipitation of calcite can be calculated according to the following equation (Appelo and Postma 2004):

$$R = r \cdot \frac{A_0}{V} \cdot \left(\frac{m_t}{m_0}\right)^n \cdot g(C), \tag{7}$$

where R is the overall reaction rate (mol/(L · s)), r specific reaction rate (mol/(m^2 · s)), A_0 calcite surface area (m^2), V volume (m^3), m_0 initial moles of calcite (mol), m moles of calcite at a given time (mol), and n factor which accounts for the change of the surface/volume during dissolution (for cubes or spheres: n = 2/3). The parameter g(C) accounts for effects of the solution composition on the rate. This can be pH, distance from equilibrium, and effects of catalysis and inhibition (Appelo and Postma 2004; Ganor and Lasaga 1998).

Calcite scales are observed at different parts of the geothermal cycle. Figure 1 illustrates a schematic geothermal facility with hydrogeochemical modeling points (1 - 9) used in this manuscript. It also shows key processes, and photographs of typical scales at each section.

Simulation point 1 denotes the geothermal reservoir, where the rock, water and gases are in thermodynamic equilibrium (SI = 0) (Wanner et al. 2017). When the water is lifted towards the surface, the hydrostatic pressure decreases, and the partial pressure of CO_2, ($p(CO_2)$), decreases slightly due to changes of the molar volumes and activity coefficients (Tanger and Helgeson 1988; Shock et al. 1992; Parkhurst and Appelo 2013; Hörbrand et al. 2018). The decreasing partial pressure of CO_2 leads to increasing pH, increased calcite SI, and to an increasing potential for calcite scale formation.

In the lower casing below the pump (between simulation point 1 and 2), where the pressure is high, no scale is observed. The pipes show rather traces of corrosion caused by H_2S than scales. This corrosion results in a layer of iron sulfides on the pipes (Wanner et al. 2017). Higher in the production casing but still below the geothermal pump, the partial pressure of CO_2 has decreased enough to produce small amounts of scale inside the pipes. Additionally, scale pieces can be found there that formed at the pump and settled down. To our knowledge, scales below the pump have not yet been investigated in the BMB.

When the thermal water touches the hot surface of the ESP motor (simulation point 2), scale formation is additionally promoted by the reduced calcite solubility at increased

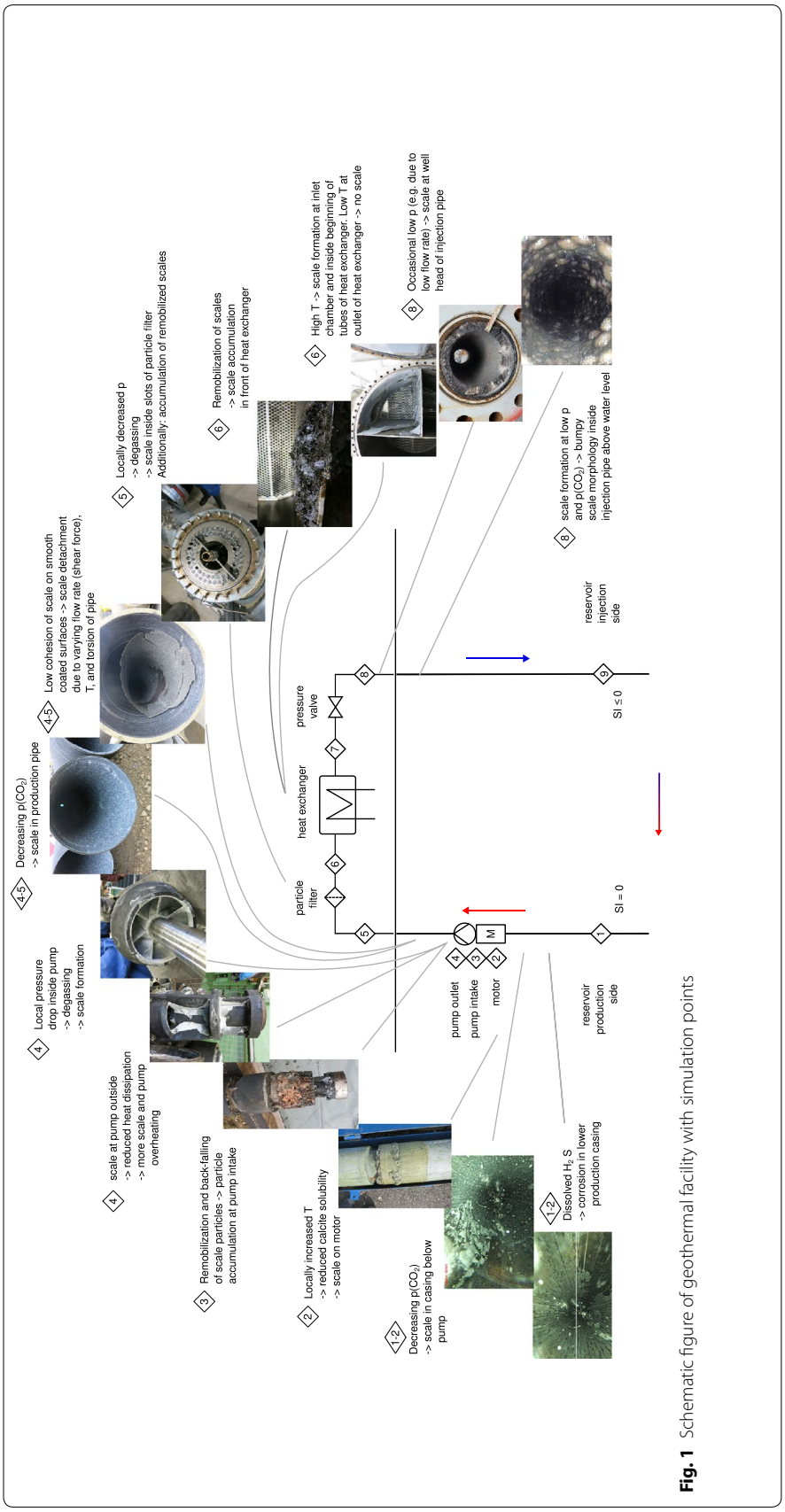

Fig. 1 Schematic figure of geothermal facility with simulation points

temperature. To our knowledge, no detailed studies on scale at the motor in the BMB are available.

For the investigation of scales at the ESP, the sampling location matters. At the pump intake (simulation point 3), remobilized scale particles accumulate and are additionally cemented together by new calcite precipitation. Scales from this part have been investigated at one site by Wanner et al. (2017).

Scales inside the ESP (between simulation points 3 and 4) have been analyzed at one site each by Wanner et al. (2017), and Herbrich et al. (2015), and are caused by decreased partial pressure of CO_2 and degassing due to a pressure drop during acceleration of the fluid in the first few pump stages (Wanner et al. 2017). Scales at the outside of the ESP, where the water is less exchanged than inside or below the pump, have been investigated at one site by Herbrich (2016).

Scales in the production pipes (between simulation points 4 and 5) have been investigated at two sites (Wanner et al. 2017; Boch et al. 2017) and at one other site (Herbrich 2016; Herbrich et al. 2015). The latter reported an increase of scale thickness towards the wellhead. Degassing in the pump is also considered to be the main cause of scales in the production pipes and the ground-level facilities in front of the heat exchanger (Wanner et al. 2017).

Scales at the filters (between simulation points 5 and 6) are reported from Boch et al. (2017). Local pressure inside the filter elements can cause degassing and accelerated calcite scale formation.

Scales at the heat exchanger (between simulation points 6 and 7) have been investigated at two sites by Boch et al. (2017).

Nothing is published so far about scales at the cold side behind the heat exchanger (simulation point 7) and the subsequent injection pipes (simulation point 8).

The theoretical thermodynamic processes of scale formation are for the most part understood. Calcite scales are formed either by a reduction of the CO_2 partial pressure or by an increase of the temperature (Schröder and Hesshaus 2009; Merkel and Arab 2018).

However, the kinetics of scale formation have only been determined at two isolated sites (Wanner et al. 2017; Herbrich 2016) and the authors did not come up with practical quantitative correlations and predictions of the scale rate based on the operational parameters and hydrochemistry. The kinetics of scale formation in geothermal facilities are particularly hard to predict because many parameters change simultaneously, i.e. pressure, temperature, the occurrence of gas bubbles, and the flow velocity. For instance, stripping and redissolution kinetics of CO_2 are dynamic effects which can until now only be monitored at the wellhead so that processes in the production pipes could not yet be quantified (Wanner et al. 2017).

Furthermore, until now, no one investigated if the scale process in geothermal facilities is surface-reaction limited or transport-limited according to the nomenclature of Appelo and Postma (2004). This has strong implications for scale prediction and for the operation of the facilities, because it indicates whether increased production rates will increase the scale rate.

The kinetic inhibiting effect of Mg^{2+} ions is an additional parameter that is generally well known from the literature (Gutjahr et al. 1996; Zhang et al. 2001). Zhang et al.

(2001) investigated scale formation by blocking experiments at a pH of 5.9 to 7.5 and a pressure of 10 - 100 bar. They found a reduction of the growth rate of calcite by 40 % when the Ca/Mg ratio was decreased from 10 to 2.5. This inhibitory effect is not yet quantitatively implemented in hydrochemical models, even though the factor C in Equation 6 could be used for this. Therefore, this inhibitory effect needs to be determined for every new setting. Moreover, other species can inhibit calcite kinetics, as well, e.g. iron, sulphates, phosphates (Appelo and Postma 2004; Gutjahr et al. 1996), and organic acids (Sanjuan and Girard 1996). In addition, shear stress can inhibit scale formation (Richard and Speck 2015; Zhao and Chen 2013; Karabelas 2002; Andritsos et al. 1997).

Considering the scarce data and knowledge on scale kinetics in geothermal facilities in the BMB, there is a need for empirical investigation of scale rates at all sections, comparison of these scale rates between different geothermal sites, and the prediction of these scales. Therefore, the objective of our study is to explore the drivers of scale formation and facilitate the prediction of rates by an empirical investigation of unprecedented detail, including 16 experimental sites in the BMB, and one from the adjacent Austrian Molasse Basin.

These goals are approached by direct scale thickness measurements, morphological investigations including crystal size measurements, and by the analyses of the hydrochemistry and gases throughout the facilities. Hydrogeochemical modeling with PHREEQC is used to calculate saturation indices, pH, the degassing pressure, and the scale rate. Furthermore, correlations of different hydrochemical and operational parameters with the scale rate are tested. Empirical regressions are derived that allow the prediction of scale rate based on hydrochemical analyses and operational parameters. Finally, the regressions are validated at other sites.

Materials and methods

Description of the facilities

Table 1 summarizes the occurrence of scales and the related operational parameters. While the production temperatures vary from 63 to 140 °C, the injection temperatures are generally around 60 - 70 °C. However, injection temperatures can be temporarily as high as the production temperature when water is bypassed at the ground level due to maintenance or low heat demand. All investigated 17 facilities exploit the same aquifer, and 13 show scales. These scales are dominated by calcite (> 95 %), which in most cases occur on the production side. 10 out of 11 facilities with production temperatures > 97 °C and production rates > 50 L/s have calcite scales. Furthermore, also 4 out of 5 facilities which produce electricity or combined heat-electricity show scales. The injection pressure at 7 out of 8 facilities is maintained at a very low level (< 2 bar). At facility 17, the fluid is continuously injected by a pump. The facilities differ widely in the depth of the reservoir. The production rates of the facilities range widely from 4 to 155 L/s, and some facilities have also a seasonal variation adapted to the heat demand. The maintained ground-level pressures differ from 5 to 22 bar. Moreover, the thermal waters contain different amounts of natural oil. However, this was not quantified or characterized, in this study.

Table 1 Occurrence of scales at geothermal facilities in the BMB indicating operational parameters, sorted by water groups according to Table 2

Site no.	Type of facility	T prod., °C	T inj., °C	Q prod., L/s	p groundl., bar	p inj., bar	Top Malm (TVD), m	Scales
13	Heat	85		84	11		2130	
15	Heat	63		26	8		1815	Fe-sulf.
17	Heat-electr.	114	57	155	13	10	4535	cc, Fe-sulf. Cu-sulf., apatite
8	Heat-electr.	140	45	100	8	<2	3773	cc, vat, Fe-sulf.
10	Electr.	137	50	135	13	<2	3485	cc, Fe-sulf., Cu-sulf.
7	Electr.	132		73	11	<2	3200	cc, Fe-sulf.
9	Electr.	132		135	14	<2	3330	cc, Fe-sulf., Cu-sulf.
16	Heat	105		30	5		2300	
5	Heat-electr.	128	45-60	125	11	<2	3150	cc Fe-sulf., Cu-sulf.
6	Heat-electr.	123	58	111	9	<2	2986	cc, Fe-sulf., Cu-sulf.
2	Heat	87		80	12		2170	
3a	Heat	104	66	50	20		2818	cc, Fe-sulf.
3b	Heat	99	66	33	18		2946	cc, Fe-sulf.
18	Heat-electr.	98		60				cc
12	Heat	93		40	11	<2	2509	
14	Heat	88	70	70	17		1970	
1	Heat	83		4	22		2400	

Type of facility = heat, electricity, or combined heat-electricity, T prod. = production temperature, T inj. = injection temperature, Q prod. = production rate, p groundl. = ground-level pressure, p inj. = injection pressure. TVD = true vertical depth. Type of scales: cc = calcite, vat = vaterite, Fe-sulf. = iron sulfides, Cu-sulf. = copper sulfides

Scale sample collection and scale measurement

Scale samples were collected during maintenance works of the geothermal facilities from all affected and accessible sections of the geothermal cycle. In total, 13 geothermal pumps, 6,000 m production pipe (sample interval 10 - 12 m), 11 heat exchanger revisions, 2 injection pipes and numerous filter elements were sampled, analyzed and evaluated. A focus was set on the investigation of the production pipes, which provides insights into the development of scale rates from the pump at 600 -1,000 m depth up to the wellhead. Regarding the production pipes, the dataset consists of six geothermal facilities, of which four have been analyzed over two or three pump changes. The scale thickness was determined by averaging at least three sliding caliper measurements at different positions of the same sample location. Samples were registered, packed individually and stored for further analyses.

At one site (site 6), scales in the casing surrounding the ESP and below, were evaluated based on multifinger caliper measurements (MFC). This is the only available source of information about scale in these inaccessible pipes, where neither scale sample collection nor direct measurements are possible. The MFC reached down to a depth of 3,000 m. The scale gauge of the lower casing was deduced from the difference to a MFC conducted 5 years before.

Analytical methods

The main part of the analyses of the scale samples was done by scanning electron microscopy with energy-dispersive X-ray spectroscopy (SEM-EDX). SEM-EDX provides morphological data, element spectra, and visualization of the microstructure. Before the measurement, samples with a high oil content were rinsed with n-hexane (Chemsolute, min. 99 %) about five times to remove any oil. Oil removal was necessary for all samples of facilities 3a, 3b, and 6, and for some of the pump and motor samples of the other facilities. The samples were then rinsed with ultrapure water once or twice and dried in a desiccator for a few days to remove residual moisture. After sputtering a gold layer onto the samples, they were visualized by SEM (Tescan Vega, 3 LM, Software: Vega TC, Kohoutovice, Czech Republic), and measured by EDX (EDX Oxford Instruments, x-act, Software: Aztex, Austin TX 78744, USA). Mineralogical data were validated using X-ray diffraction (XRD) and Raman micro-spectroscopy. The SEM-EDX images were processed with ImageJ (Schindelin et al. 2012) to measure the pore- and crystal size distribution. The crystal size is of particular interest, since it is reported to correlate with supersaturation (Beck and Andreassen 2012; Larsen et al. 2006). Hence, we tested whether the crystal size could be used as an indicator of the prediction of scale rates. For quantitative elemental analysis, microwave hydrochloric acid digestions (36 %) of the scales were conducted by heating the sample for 30 min at 220 °C. After cooling and diluting, cations were detected by ICP-MS (PerkinElmer, NexION 350D).

Water and gas composition

At 13 of the facilities, the hydrochemical composition of the geothermal water was analyzed. Water and gas samples were collected at temperatures ranging from 30 - 75°C, consistently at 1.0 bar absolute pressure. For this, the water was cooled down by a chilling-unit connected to the pipes in front of the automatic filter (point 5 in Figure 1). The pH value, temperature, electric conductivity, and redox potential were measured on-site (InLab Expert Go-ISM resp. InLab 738-ISM resp. InLab Redox ORP, Mettler-Toledo, Germany). Dissolved CO_2 and acid capacity were analyzed by titration in the field (0.1 M HCl (Carl Roth), 0.1 M NaOH (Carl Roth)), and the colorimetric indicators phenolphthalein (Merck) and cooper (Sigma-Aldrich)). In the lab, anions were quantified by IC (Dionex, IC25). Calcium was determined by EDTA titration. The other cations were determined by AAS (PerkinElmer, 3300), and AES (ELEX 6361, Eppendorf). The gas loading (gas volume per water volume) was determined at 1.0 bar pressure and temperatures ranging from 30 - 75°C by an on-site degassing unit as described in Baumann (2016). By the use of ideal gas law, the gas loading was normalized to standard conditions (1.013 bar, 0°C) and indicated as NmL/L. During the on-site degassing, gas samples (1 L glass) were taken, and the composition was later analyzed by GC–MS (Shimadzu GCMS-QP2010 Ultra, Kyoto, Japan) with helium as carrier gas.

Hydrogeochemical modeling

Based on the method of Baumann (2016) which uses numerical back-calculation of hydrochemistry to reservoir conditions, $SI_{calcite}$, pH, and degassing pressure were calculated for the wellhead (point 5 in Figure 1) at six representative facilities with the software PHREEQC and the phreeqc.dat database (Parkhurst and Appelo 1999). The

back-calculation to reservoir conditions (point 1 in Figure 1) is required since water and gas samples taken at the surface at ambient conditions have changed compared to the physical and chemical conditions present in the pipes. In PHREEQC, the pressure effect on partial pressure of CO_2 and $SI_{calcite}$ is incorporated by the SUPCRT-modified-Redlich–Rosenfeld (SmoRR) equation, which is a complex function of temperature, pressure, and solution composition (Parkhurst and Appelo 2013). The model includes the main inorganic species related to carbonate equilibria ($CO_{2(g)}$, $CO_{2(l)}$, $CaCO_3$, HCO_3^-, $CaHCO_3^+$, $CaOH^+$, $CaSO_4$, $MgCO_3$, and $MgHCO_3^+$), but does not include hydrocarbons. The models for the six selected facilities are consistent since the back-calculation yields the measured fluid composition for sampling conditions at the wellhead. The degassing pressure represents the pressure at which a free gas phase forms in the geothermal pipes. A minimum gas volume of 0.01 mL/L was defined to show the degassing pressure. Scale rates were modeled by Equation 6 (Plummer et al. 1978), which is implemented in phreeqc.dat and attached in the (Additional files 1). The surface-to-volume-ratio was calculated from the pipe geometries.

Calculation of scale rates and mass balance

The scale rates are calculated in mol/($m^2 \cdot s$) treating the scale as pure calcite with a density of 2.710 g/cm^3 (Tegethoff 2013), despite the small portion of incorporated magnesium. For the production pipes, the attachment surface of the precipitates refers to the inner cylindrical surface, and the time refers to the time period between installation and extraction of the pipes. The rates in the production pipes were correlated to the pressure resulting from hydrostatic pressure and wellhead pressure.

By comparison of the mass of calcite scale along the production pipe to the ion concentrations of calcium and hydrogen carbonate measured at the wellhead, the relative change of the hydrochemical composition during rise in the production pipe was calculated. It was tested if the amount of scale can be deduced from variations of ion concentrations at the wellhead.

Parameter analysis

To quantify the influence of each hydrochemical or operational parameter, the scale rate at the wellhead was related to each parameter. At the wellhead, scale thickness can be measured best due to the highest thickness, and the effect of the geothermal pump on the scale rate is less strong than in the rest of the production pipe (Herbrich 2016). Therefore, hydrochemical and operational parameters can be studied best at the wellhead.

Results and discussion

Analysis of hydrochemical composition

Table 2 shows the hydrochemical analyses of the investigated facilities. The charge balance of all samples is <5 %. Waters were sorted into groups based on TDS, Ca/Mg, and geographic location (weighed in this order). Here, the ratio Ca/Mg indicates a dolomitic reservoir for group 1 and a limestone reservoir for groups 2 – 4 (Langmuir 1971).

The ratio $(Na^+ + K^+ - Cl^-)/HCO_3^-$ serves as a quantitative indicator of cation exchange where Ca^{2+} and Mg^{2+} exchange with Na^+ or K^+ incorporated in clay minerals

of higher strata. The ratio is high, if ion exchange occurred (strongest in group 2) or if the concentration of other anions (sulphuric species) is high (group 4).

The ratio of $(S^{2-} + HS^{-})/SO_4^{2-}$ serves as quantitative parameter for the redox-conditions.

Scale occurrence, composition, and morphology

All facilities except for facilities 2, 13, and 16 have scales. The SEM-EDX measurements showed that averaged over all sections of the affected facilities, > 95 % (mass percent) of the scales consist of calcite with some incorporation of magnesium. Mineralogical differences between the different sections of the facilities only concern accessory minerals. The Ca/Mg ratio of the scales in the investigated plants is in the range of 11 - 16. The results were confirmed by XRD, transmitted light microscopy, Raman micro-spectroscopy, and acid digestion.

Modeled hydrochemical parameters

A hydrogeochemical model was established for six selected facilities as an example. For these sites, pH and $SI_{calcite}$ at the wellhead were calculated. At first glance, and without any additional operational parameters, almost no correlation can be seen between hydrochemistry and scale occurrence. Only the low $SI_{calcite}$ of site 16 correlates with absence of scale.

Measured gases and modeled degassing pressure

Figure 2 shows the high variability of gas loads, gas composition, and the calculated degassing pressure. Gas loads range from 10 to 360 NmL/L. At the applied degassing pressure of 1.0 bar, the gas composition is dominated by CH_4 with 46 - 75 % by volume. Samples with high CH_4 content suggest influence of oil-field waters infiltrating from higher strata (Mayrhofer 2013). This infiltration is strong at facilities 2 and 3b, as can be seen from the high salinity of these sites (Table 2). Lower CH_4 contents point to less

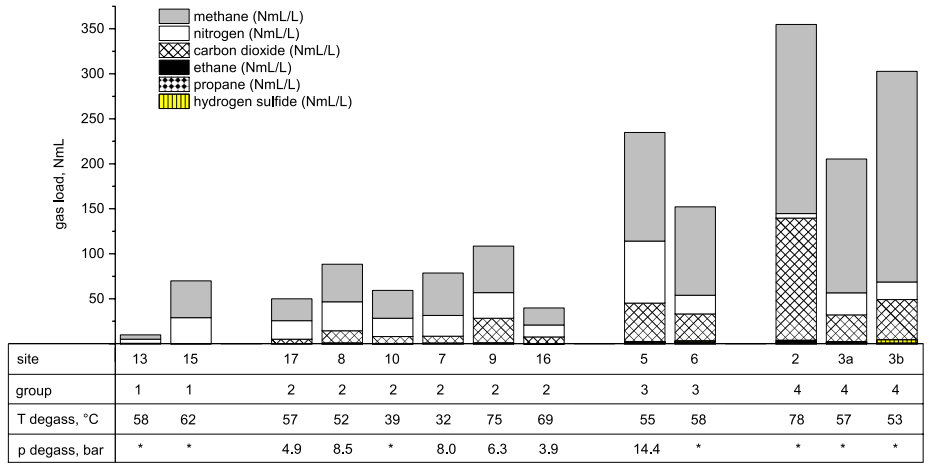

site	13	15	17	8	10	7	9	16	5	6	2	3a	3b
group	1	1	2	2	2	2	2	2	3	3	4	4	4
T degass, °C	58	62	57	52	39	32	75	69	55	58	78	57	53
p degass, bar	*	*	4.9	8.5	*	8.0	6.3	3.9	14.4	*	*	*	*

Fig. 2 Normalized gas load and gas composition with indication of degassing temperature during sampling (p = 1.0 bar). The degassing pressure is calculated for the production temperature given as p degass. *No data for back-calculation

Table 2 Analysis of geothermal waters at the wellhead of the investigated facilities

Group	Site Nr.	TDS (mg/L)	CO_2 (mmol/L)	HCO_3^- (mmol/L)	Ca^{2+} (mmol/L)	Mg^{2+} (mmol/L)	Ca/Mg (mmol/mmol)	Scales
1	13	634	2.11	5.20	0.93	0.39	2.4	
1	15	680	2.00	5.90	0.96	0.45	2.1	Fe-sulf.
2	17	661	2.00	4.11	0.85	0.18	4.6	cc, Fe-sulf., Cu-sulf., apatite
2	8	656	4.79	4.23	0.42	0.09	4.5	cc, vat, Fe-sulf.
2	10	548	1.80	4.52	0.25	0.08	3.0	cc, Fe-sulf., Cu-sulf.
2	7	648	2.70	3.36	0.58	0.12	5.0	cc, Fe-sulf.
2	9	605	4.79	4.33	0.51	0.11	4.6	cc, Fe-sulf., Cu-sulf.
2	16	689	2.60	4.92	0.71	0.18	3.9	
3	5	917	4.41	5.08	1.09	0.25	4.4	cc
3	6	902	4.80	4.98	0.85	0.23	3.7	cc, Fe-sulf., Cu-sulf.
4	2	4844	3.91	7.24	3.57	1.29	2.8	
4	3a	1109	3.00	12.85	1.05	0.24	4.3	cc, Fe-sulf.
4	3b	2083	5.02	5.00	2.36	0.75	3.1	cc, Fe-sulf.

Group	Site Nr.	$(Na^+ + K^+ - Cl^-)/HCO_3^-$ (meq/meq)	$(S^{2-} + HS^-)/SO_4^{2-}$ (meq/L)	pH*	SI calcite*	Water type	Scales
1	13	0.56	0.54	**	**	$Na - Ca - HCO_3 - Cl$	
1	15	0.57	0.74	**	**	$Na - Ca - HCO_3 - Cl$	Fe-sulf.
2	17	0.61	0.58	6.75	0.30	$Na - Ca - HCO_3 - Cl$	cc, Fe-sulf., Cu-sulf., apatite
2	8	0.84	1.00	6.72	0.24	$Na - HCO_3 - Cl$	cc, vat, Fe-sulf.
2	10	0.92	0.66	**	**	$Na - HCO_3 - Cl$	cc, Fe-sulf., Cu-sulf.
2	7	0.70	0.99	6.66	0.22	$Na - HCO_3 - Cl$	cc, Fe-sulf.
2	9	0.69	0.76	6.69	0.20	$Na - HCO_3 - Cl$	cc, Fe-sulf., Cu-sulf.
2	16	0.67	0.61	6.73	0.17	$Na - HCO_3 - Cl$	
3	5	0.59	2.06	6.42	0.23	$Na - Ca - HCO_3 - Cl$	cc, cc

Table 2 Continued

Group	Site Nr.	$(Na^+ + K^+ - Cl^-)/HCO_3^-$ (meq/meq)	$(S^{2-} + HS^-)/SO_4^{2-}$ (meq/L)	pH*	SI calcite*	Water type	Scales
3	6	0.44	1.89	**	**	Na – Cl – HCO_3	cc, Fe-sulf., Cu-sulf.
4	2	0.82	8.11	**	**	Na-Cl	
4	3a	0.67	1.86	**	**	Na – Cl – HCO_3	cc, Fe-sulf.,cc
4	3b	0.29	4.00	**	**	Na – Cl – HCO_3	cc, Fe-sulf.,cc

Total dissolved solids = TDS. * = calculated values. **No data for back-calculation. Four groups of geothermal waters can be distinguished: 1) low-saline dolomite in the northeast of Munich, 2) low-saline limestone southeast of Munich, 3) medium-saline limestone southeast of Munich, 4) high-saline gas-rich western Molasse Basin. Water type = according to Furtak & Langguth (1965)

infiltration from higher strata. The other two major gas components are N_2 with 1 - 46 % and CO_2 with 0 - 39 %. It is important to note that the gas composition is highly dependent on the degassing pressure during sample collection. This explains why at other gas analyses of the same carbonate Malm waters, where degassing was conducted at roughly 30 mbar absolute pressure, the extracted gas is dominated by CO_2 (Wanner et al. 2017).

The calculated degassing pressures, where a volume of 0.01 mL/L gas phase forms in the fluid, vary between 3.9 and 14.4 bar for the six modeled facilities. The rest of the gases (ethane, propane and H_2S) contribute only minor portions to the gas mixture. The gas load has a temporal variation, too, which is reported to be in the range of $\pm$ 20 % over one year (Wanner et al. 2017). These variations are much stronger for CH_4 and N_2 than for CO_2 (Wanner et al. 2017). Inside the central BMB, a generally increasing trend of the gas load from east to west and from north to south can be observed from our data. The western BMB is excluded from that trend (sites 2a, 2b and 3).

Despite the small portion, H_2S is considered to be the main corrosive gas in the system since the steel surfaces are covered by iron sulfides representing the corresponding corrosion product (Wanner et al. 2017; Herbrich 2016; Boch et al. 2017). Dissolved CO_2 partly forms H_2CO_3, which is also corrosive but produces iron carbonate $FeCO_3$ (Kahyarian et al. 2017), which is not observed on the pipes in the Molasse Basin. N_2 and CH_4 generally do not contribute to corrosion (Leygraf et al. 2016), (Popoola et al. 2013; Latosov et al. 2017).

Based on Figure 2, two effects on the scale rate are expected: The first effect has a thermodynamic rationale, postulating a dependence of the scale rate on the CO_2 partial pressure. This means that the decrease in CO_2 partial pressure due to decompression in the pipe is greater if the CO_2 makes up a larger portion of the gas composition. The second effect on the scale rate is a kinetic effect due to CO_2-stripping into gas bubbles which formed due to degassing of gases with lower solubility, e.g. CH_4 or N_2. This means that removal of CO_2 is kinetically favoured if gas stripping occurs, no matter which gas is the first one to start degassing. This effect is also active when the proportion of CO_2 in the total gas is small. The stripping effect would be accelerated at higher gas loads. This leads to the question whether scale formation can be predicted based on thermodynamic drivers (effect 1, i.e. CO_2 partial pressure) or whether kinetic effects (effect 2, i.e. CO_2 stripping and Mg-inhibition) must be considered, too. This question is elucidated in the following sections.

Scale drivers

To provide a basis for subsequent correlations with scale formation, Figure 3 summarizes the thermodynamic scale drivers. The Figure shows how the hydrochemistry changes on the way from the reservoir (black bars) to the wellhead (blue bars), as calculated with PHREEQC for the six modeled facilities. Since the water is in carbonic acid equilibrium in the reservoir (Wanner et al. 2017), the shift of the parameters is crucial for calcite scale formation, but not the absolute value of the parameters. For a better comparison of the sites and the general scale susceptibility, the hydrochemistry is also modeled for a so-called standard wellhead of 5 bar (red bars).

Some parameters (pressure, CO_2 partial pressure, pH, $SI_{calcite}$) experience a shift on the way up to the wellhead. Other parameters (temperature, Ca^{2+} concentration, and

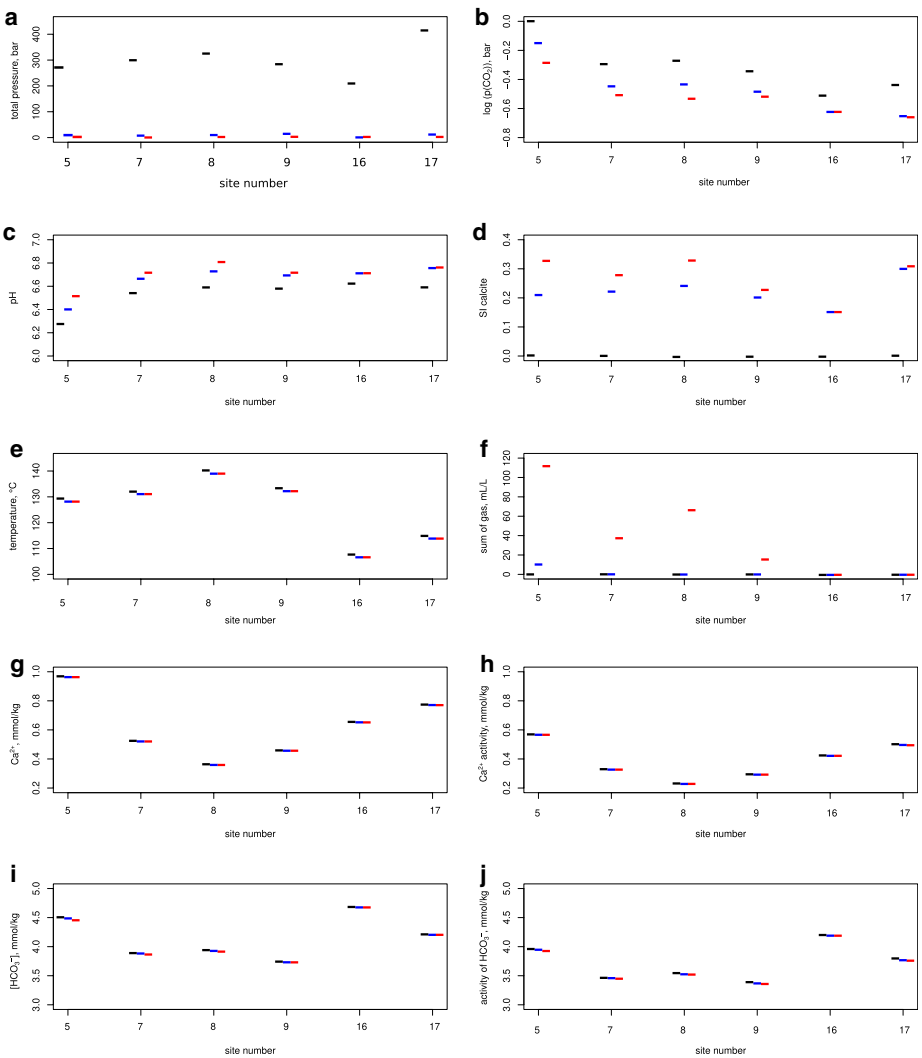

Fig. 3 Scale-driving parameters at reservoir pressure (black bars: simulation point 1 (according to Fig. 1)), at standardized wellhead pressure at 5 bar (red bars: simulation point 5), and at real wellhead pressure at 5–14 bar (blue bars: simulation point 5). X-axis shows site number. **a** total pressure, **b** logarithmic partial pressure of CO_2, **c** pH, **d** $SI_{calcite}$, **e** temperature, **f** sum of free gas phase, **g** calcium ion concentration, **h** calcium ion activity, **i** bicarbonate ion concentration, **k** bicarbonate ion activity

Ca^{2+} activity, as well as HCO_3^- concentration and HCO_3^- activity), however, stay more or less constant. The sum of free gas load experiences a shift (increase), too, if the wellhead pressure is below degassing pressure.

Due to the minimal temperature difference (< 2 K), the pressure effect is expected to be the dominating driver of the $SI_{calcite}$, despite the high sensitivity of calcite $SI_{calcite}$ on temperature. The small temperature difference during normal production is also confirmed by Bauer et al. (2014).

The scale driver $p(CO_2)$ and hence the $SI_{calcite}$ can be shifted by two different processes (Figure 3). The first process is that $p(CO_2)$ is shifted due to the total pressure contrast (blue bars at facilities 7, 8, 9, and 17). Then the amount of $p(CO_2)$ shift depends on the

Table 3 Time period of pipe installation, depth of pipe below surface, scale rates at the wellhead, produced water volume = Q, calcium ion concentration [Ca^{2+}] measured at the wellhead, and scale-related decrease of calcium ion concentration [%] in the production pipes and underlying casing

Site	Time Period	Pipe, m	Rate wellhead, μmol/($m^2 \cdot s$)	Q, Mio. m^3	[Ca^{2+}], mmol/L	Δ [Ca^{2+}], %
10	07/2016 –03/2017	970– 0	1.7	2.0	0.25	1.71
9**	12/2014–03/2015	800–0	2.8	0.7	0.51	2.14
9	10/2016–03/2018	680–0	3.0	5.6	0.51	1.50
9	10/2012 - 03/2018	980–680	2.5	16.2	0.51	0.80
8*	10/2012–03/2013	860–0	2.4	0.6	0.42	3.40
8*	08/2013–12/2013	860–0	3.2	0.7	0.42	1.50
8*	12/2013–09/2014	860–0	2.4	1.9	0.42	2.50
7	15/2015–02/2017	520–0	1.6	1.7	0.59	1.25
17	11/2016–10/2017	670–0	3.8	4.1	0.85	1.68
6	12/2013–11/2016	880–0	1.9	3.0	0.93	0.72
6	12/2015–06/2017	880–0	1.9	4.9	0.93	0.69
6	08/2010–12/2015	1800–850	1.0	16.9	0.93	1.10

Calculations marked with * and ** are based on gauge measurements of Herbrich (2016), respectively Wanner et al. (2017)

pressure drop between reservoir and wellhead, and on the initial $p(CO_2)$. The other process is that $p(CO_2)$ and $SI_{calcite}$ are shifted due to a high total gas load (see also Figure 2). This high gas load promotes CO_2-stripping, even when the pressure contrast between reservoir and wellhead is low. This second process becomes particularly important at low wellhead pressures. This can be seen from the $SI_{calcite}$ at standardized wellhead pressure (red bars), which is significantly higher than the $SI_{calcite}$ at real wellhead pressure (blue bars) for facilities 5, 7, 8, and 9. Site 5 is the only site, where CO_2-stripping is already active at real wellhead pressure (blue bars).

Mass balance

In a next step, we tested by a mass balance approach, whether scale formation can be derived from hydrochemical samples at the well head. Table 3 summarizes the scale rates at different sections of all investigated sites with a full data set of scale rates from the ESP to the wellhead. Facilities 6 and 9 provide, in addition, also the scale rate below the ESP. Also shown in Table 3 is the resulting reduction of the calcium ion concentration due to scale formation. The results show that hydrochemistry changes only little on the way up, since only 0.7–3.4 % of the dissolved calcium ions precipitate. On the average, the calcium ion concentration decreases by 0.8–1.0 % on the ascent from the reservoir to the pump. This lies within the analytical errors, and implies that scale formation cannot be directly monitored by hydrochemical analyses at the wellhead. Instead, thickness measurements of scales are indispensable.

This finding is in contrast to earlier studies (Wanner et al. 2017) who measured strong variations of the calcium ion concentrations (from 0.10 mmol/L to 0.48 mmol/L) at the wellhead during 10 measurements distributed over one year. The authors concluded that these variations are caused by varying calcite precipitation. Our mass balance

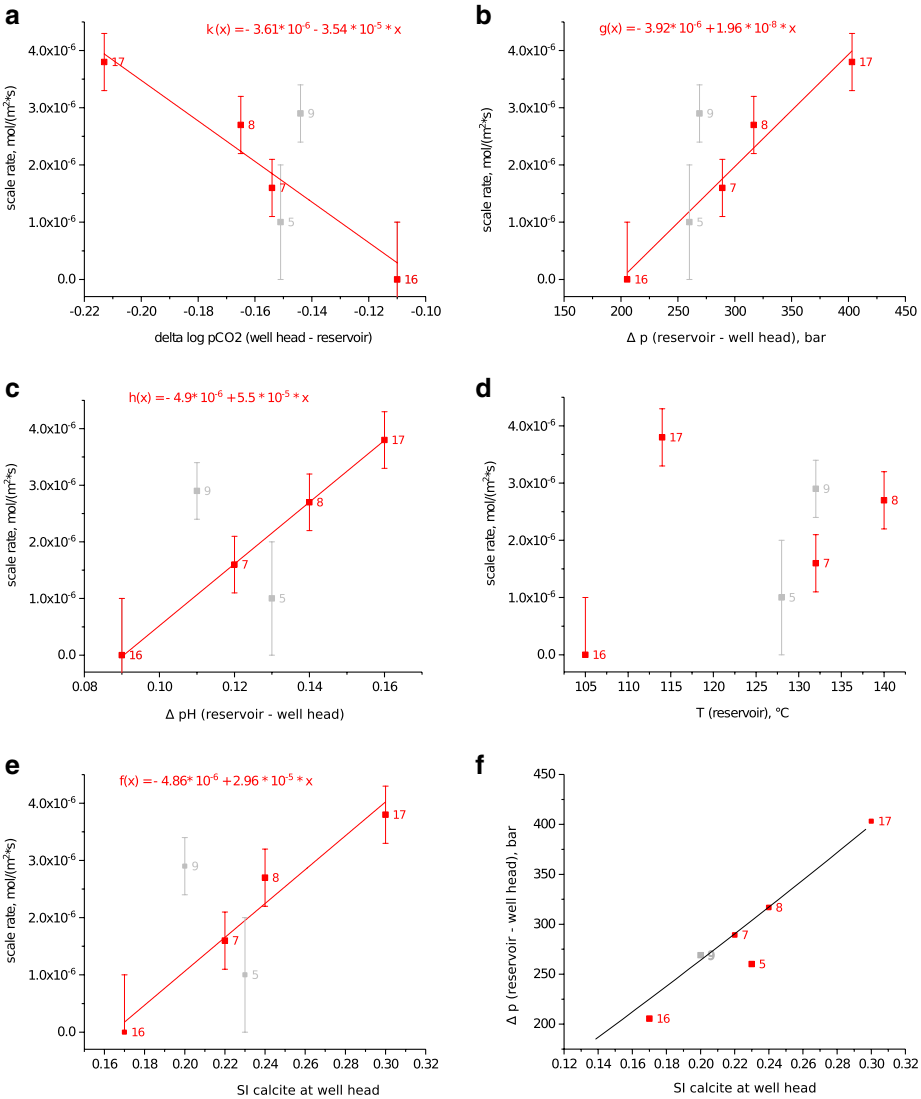

Fig. 4 Correlations between scale rate at the wellhead of the production pipe and different parameters with indication of error bars. Data points labeled with site number. Red data points: reliable data. Grey data points: less reliable or particular data (site 9: many different pumps, site 5: scale thickness according to facility operator). **a** Scale rate against Δ log (pCO2) between reservoir and wellhead. **b**) Scale rate against Δ between reservoir pressure and wellhead pressure. **c**) Scale rate against Δ pH between reservoir and wellhead. **d**) Scale rate against reservoir temperature. **e**) Scale rate against $SI_{calcite}$ at the wellhead. **f**) Δ between reservoir pressure and wellhead pressure against wellhead $SI_{calcite}$. The black line shows the theoretical pressure dependence of $SI_{calcite}$ as calculated with PHREEQC. Linear regressions k(x), f(x), g(x), and h(x) between parameters and scale rate

demonstrates that scaling effects cannot be derived from hydrochemical samples at the wellhead. The variations of the hydrochemistry at the wellhead are more likely caused by time-dependent variable dissolved ion concentrations, different proportions of infiltrating waters from higher geological strata, or by changes of the flow dynamics in the reservoir. The small calcium ion depletion on the way through the production pipe, coupled with fully turbulent conditions, has also an implication on the scale limiting process. It

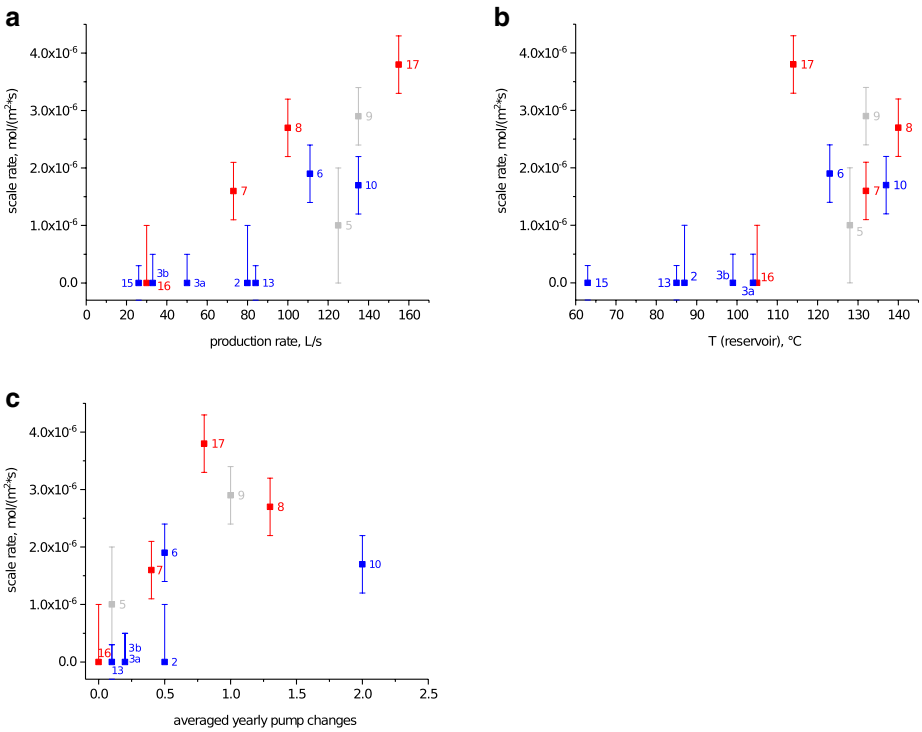

Fig. 5 Correlation between scale rate at the wellhead (mol/(m^2 · s)), production rate (**a**), reservoir temperature (**b**), and frequency of pump changes (**c**). Data points labeled with site number. Red data points: reliable data. Grey data points: less reliable or particular data (site 9: many different pumps, site 5: scale thickness according to facility operator). The dark blue data points are the observed scale rates at facilities where hydrochemical analyses but no hydrochemical model were available

suggests that mass limitation can be ruled out as the scale-limiting process. Instead, the surface-reaction kinetics are the limiting factor.

Suitable parameters for scale rate prediction

The driving forces of scale formation identified in Figure 3 (Δ log (pCO_2), Δ total pressure, Δ pH, and $SI_{calcite}$) are plotted against the scale rate (Figure 4). Furthermore, also the reservoir temperature is plotted against the scale rate. The data points in Figure 4 are color-coded according to their validity. The red-coloured data points denote representative and reliable sites. The grey-coloured data points are less representative or less reliable. This distinction was made because the scale thickness at site 5 derives from the information of the facility operator, and was not measured by ourselves. Site 9 is marked grey, and considered special since it was subject to different experiments, where different pumps and pipe coatings were tried leading to increased scale rates. Evident correlations are observed between scale rate and the parameters Δ log (pCO_2), Δ total pressure, Δ pH, and $SI_{calcite}$. This confirms that Δ $p(CO_2)$ is the main scale driver at the wellhead, which leads to a shift of the pH and $SI_{calcite}$. Considering Δ $p(CO_2)$ a higher |Δ $p(CO_2)$| leads to higher scale rate. If Δ log $p(CO_2)$ is smaller than -0.12 scales are expected. Scale

formation is, furthermore, observed at a pH increase of at least 0.10 - 0.12. Also at a $SI_{calcite}$ > 0.16 scale occurs.

In Figure 4 f), the $SI_{calcite}$ is linked to the total pressure showing a good correlation, too. This is because the total pressure effect on the $SI_{calcite}$ is stronger than the temperature effect as explained before (Figure 3). Therefore, total pressure correlates with the scale rate, as well, with an onset of scale formation at a Δ total pressure of 200 - 250 bar.

Due to the causal correlation of the parameters Δ log (pCO_2), Δ total pressure, Δ pH, and $SI_{calcite}$ to the scale rate, empirical linear regressions were plotted in the diagrams, which can be used for scale rate prediction. Linearity of the regressions is justified due to the almost linear increase of $p(CO_2)$ $SI_{calcite}$ with decompression (see Additional file 2). The regressions are derived from the red marked data points which are considered representative for sites in the BMB.

In contrast to the other parameters, no clear correlation between scale rate and absolute temperature can be seen. This is because the strong influence of temperature on carbonate scale formation is limited to the minimal temperature loss Δ T between reservoir and wellhead (see Figure 3).

The scale rate at site 5 is lower than expected from the regression with SI and pH. This indicates that kinetic aspects play a significant role at this facility. Due to the particular slow start cycle of the ESP at this site, degassing in the pipe might be reduced compared to other sites. This could lower the scale rate. Another explanation for the low scale rate at site 5 is that in the reservoir or during rise of the fluid, mixing corrosion occurs, caused by inflow of waters from higher strata. This leads to a lower $SI_{calcite}$ than calculated in Figure 3, and the geothermal water is not in hydrochemical equilibrium with the reservoir rock.

Use of operational parameters for scale rate prediction

We have now identified the thermodynamic driving parameters for scale formation (Δ log (pCO_2), Δ total pressure, Δ pH, and $SI_{calcite}$), and have presented the measured scale rates at the wellhead. In a next step, we assessed if the operational parameters production volume, and frequency of pump changes are also suitable for scale prediction by plotting them against scale rate at the wellhead (Figure 5 a) + c)). For these plots, all 13 investigated facilities with available operational and hydrochemical data are included, also those, for which no hydrochemical model was built. For this extended data set, the easily available parameter temperature is also once again plotted against scale rate, to verify if still no correlation is observed.

Figure 5 a shows that scale rate correlates with higher production rates. However, this kinetic factor is not the main causal driver of scale formation and is hard to isolate. Yet, a higher production rate causes more turbulence due to increased Δ total pressure in the pump which kinetically promotes scale formation to an unknown extend. On the other hand, increased turbulence also promotes heat transfer to the surrounding rock, and therefore reduces scale formation. This second effect is mainly only relevant during starting phase. Thus, production rate will likely promote scale formation due to degassing but this kinetic effect cannot be quantified due to the complex interaction with other parameters.

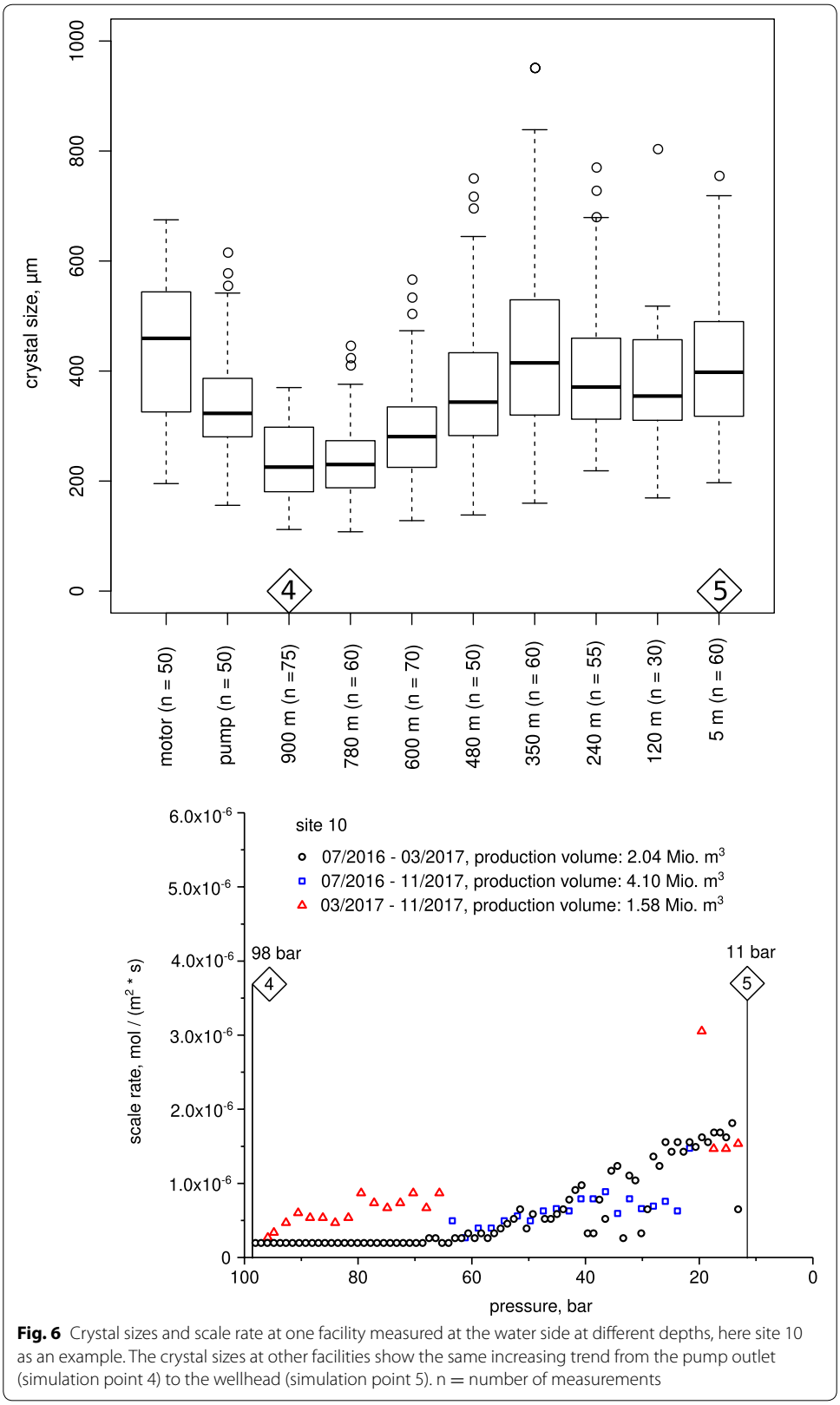

Fig. 6 Crystal sizes and scale rate at one facility measured at the water side at different depths, here site 10 as an example. The crystal sizes at other facilities show the same increasing trend from the pump outlet (simulation point 4) to the wellhead (simulation point 5). n = number of measurements

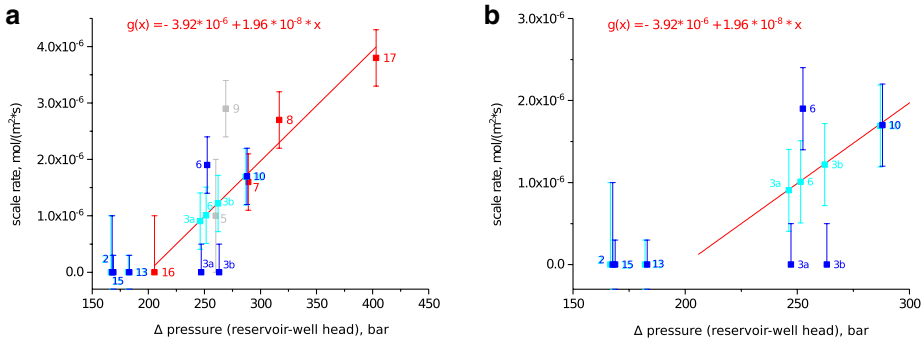

Fig. 7 Correlation between scale rate at the wellhead (mol/(m^2 · s)) and production rate (L/s). Data points labeled with site number. The dark blue data points are the observed scale rates of several facilities. The bright blue data points are scale rates of these facilities modeled by the regression $g(x) = -3.92 \cdot 10^{-6} + 1.96 \cdot 10^{-8} \cdot x$ based on Δ pressure (x). **a** (left) shows also the red and grey data points used for the development of the regression while **b** (right) shows only the new blue data points used for validation. Observed and modeled values are identical for sites 2, 10, 13, and 15

In Figure 5 b, temperature shows a correlation to scale formation. However, the true scale drivers behind this are Δ log $p(CO_2)$ and Δ total pressure as shown in the sections before. The higher temperatures are just an effect of the geothermal gradient but do not cause the scale formation. Therefore, temperature only seemingly controls the scale rate.

Figure 5 c shows that in most cases, the frequency of pump changes correlates with the scale rate. Moreover, this is, again, a co-dependency: scales cause pump failures, not the other way around. Therefore, the number of pump changes is affected by scales but is not a suitable scale predictor. The frequency of pump changes can be increased by many other technical problems than scalings, too, as it is the case for site 10.

To summarize, the parameters presented in Figure 5 only have a limited use for the prediction of the scale rate, and should not be used.

Use of crystal size for scale rate prediction

Figure 6 tests if crystal sizes can be used for scale rate prediction by linking scale kinetics to the crystal size in vertical direction of one selected site. We have seen in Figure 4 that $SI_{calcite}$ controls the scale rate, and increases towards the wellhead. Furthermore, $SI_{calcite}$ controls also the crystal size (Beck and Andreassen 2012; Larsen et al. 2006). A high $SI_{calcite}$ is expected to correlate with a high scale rate and low crystal size. However, Figure 6 shows the opposite. Here, crystal sizes between 200 - 1000 μm at the water side show an increasing trend towards wellhead. This contradiction shows that the crystal size may not be a good indicator of the scale rate.

The contradiction can be explained if film flow occurs in the upper part of the pipe. Then crystal size at the wellhead could be high due to a local low $SI_{calcite}$.

Validation of scale rate prediction at the wellhead

Figure 7 validates how well the regression based on the total pressure difference (Figure 3 b) works for the prediction of scale rates at other, not yet modeled, facilities. While

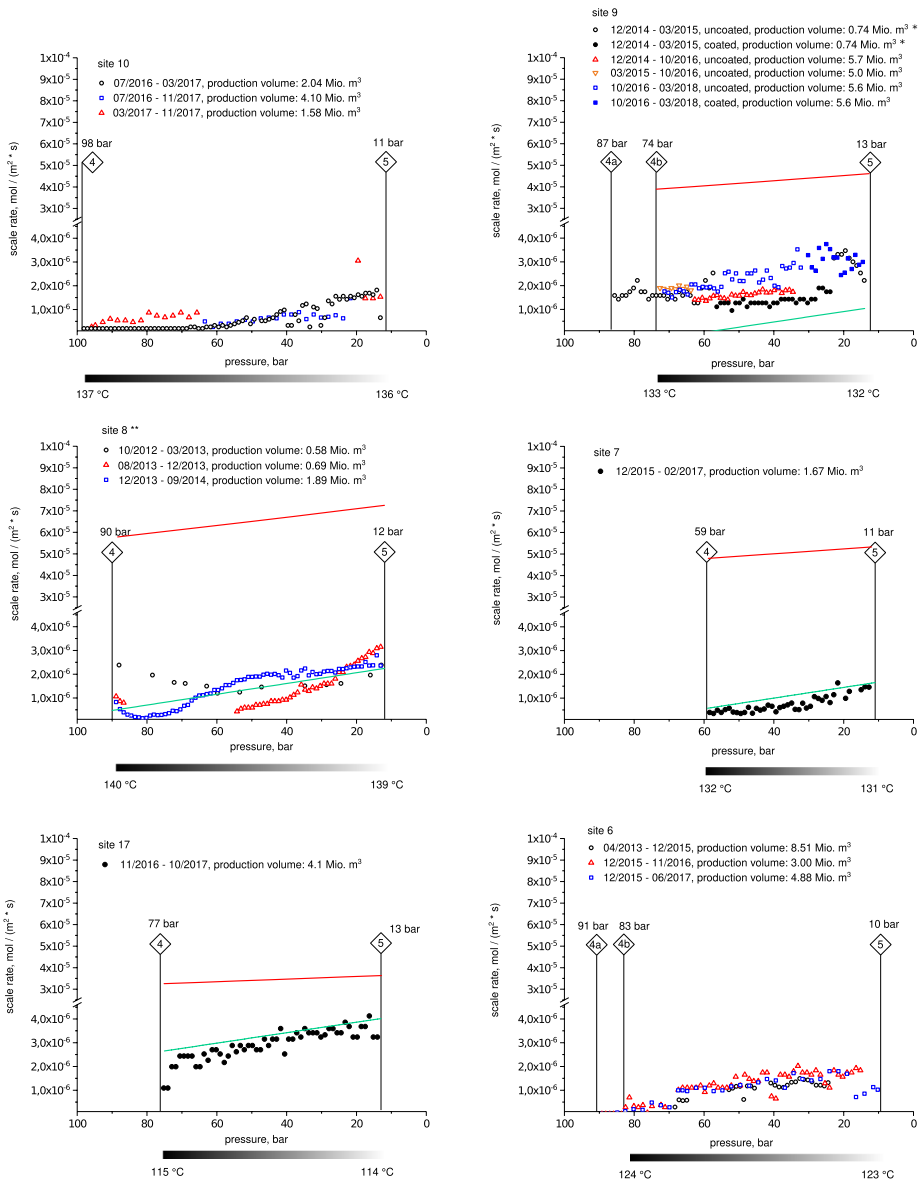

Fig. 8 Measured development and modeling of precipitation rates as a function of pressure at the investigated facilities with the indication of investigated time period, produced volume of geothermal water, fluid temperature, and modeling points. Red lines: scale rate modeled with existing hydrochemical models (PHREEQC). Green lines: scale rate modeled based on experimental regression between SI (x) and scale rate ($f(x) = -4.86 \cdot 10^{-6} + 2.96 \cdot 10^{-5} \cdot x$) at the wellhead. *Scale thickness from Wanner et al. (2017) implemented (site 9), **Scale thickness based on data from Herbrich (2016) (site 8)

for facilities 2, 10, 13, and 15, predictions work fine, facility 6 has a slightly higher scale rate than predicted, and facilities 3a and 3b plot below their modeled scale rates.

The higher scale rate at facility 6 might be due to the high number of pump changes or due to strong degassing. The reason why facilities 3a and 3b do not have scales at the wellhead of the production well even though it is predicted by the model might be that the particular high oil content in the thermal water of that site might inhibit scale formation or the attachment on the walls (Sanjuan and Girard 1996; Zhao and Chen 2013;

Karabelas 2002; Avramov 2009). However, oil was not quantified in this study, and is not implemented in the hydrochemical model, either. Furthermore, oil could also promote scale formation since oil droplets can serve as crystallization nuclei (Huang et al. 2019). If oil droplets attach to the pipes, scales can grow.

Validation of scale rate prediction along the production pipe

Until here, we have validated our regressions for the prediction of the scale rate only at the wellhead. Now, we test how well the SI-to-scale rate regression depicts the scale development along the production pipe at six facilities with a consistent hydrochemical model (Figure 8). Additionally, we also apply the scale rates suggested by Plummer et al. (1978) using PHREEQC to see if this model or our new regressions yield better results.

The observed scale rates increase from the pump to the wellhead, where they reach 1.5 - 4.1 μmol/(m$^2 \cdot$ s).

The scale rates modeled with PHREEQC show a qualitatively correct picture. Given the very small temperature gradient and the high pressure gradient, the $SI_{calcite}$ and the scale rates increase towards the wellhead, as expected.

However, the PHREEQC model fails at the quantitative simulation of the scale rates. The modeled rates are one order of magnitude higher than the measured ones. This problem could reasonably be solved by introducing a strong inhibitory factor, e.g. by modifying the surface-to-volume-ratio. Also other studies found that scale rates in real settings are often strongly inhibited by magnesium (Svensson and Wolfgang 1992; Zaihua et al. 1995; Herman and Lorah 1988). Here, also oil could have an inhibiting effect on scale formation (Sanjuan and Girard 1996; Zhao and Chen 2013; Karabelas 2002; Avramov 2009). Another explanation why the modeled rates are too high can be that the calcite precipitation kinetics implemented in PHREEQC are based on dissolution experiments, not on precipitation experiments. The backwards reaction, i.e. precipitation may happen more slowly than the dissolution reaction.

Even if the order of magnitude of the scale rate were corrected by an inhibition factor, there is a second problem of this model: the measured strong increase of the scale rate along the production pipe is not depicted by the model. The model greatly underestimates the effect of the $SI_{calcite}$ on the scale rate. This issue cannot be solved without an arbitrary modification of the $SI_{calcite}$ term in the rate equation of Plummer et al. (1978) and, therefore, without changing the whole model in a non-intended way.

While the PHREEQC model fails at predicting the scale rate, the scale rate-to-SI regression presented in Figure 4 matches more or less the measured scale rates at sites 7, 8, and 17. Site 9 has higher rates than modeled which can be attributed to many pump starts, which lead to a more frequent and stronger degassing in the ESP followed by disruption of the carbonic acid equilibrium. To summarize, the new introduced regressions can also be used for scale rate prediction along the production pipe, and are not restricted to the wellhead.

The shapes of the measured scale rate plots host also additional information which can give a hint to particularities of the sites. Some facilities show a slightly exponential scale rate increase, which deviates from the almost linear expected shape. These differences indicate kinetic effects due to degassing. As far as the degassing effects are concerned, degassing in the ESP leads to a kinetically limited stripping of CO_2 into gas bubbles, and

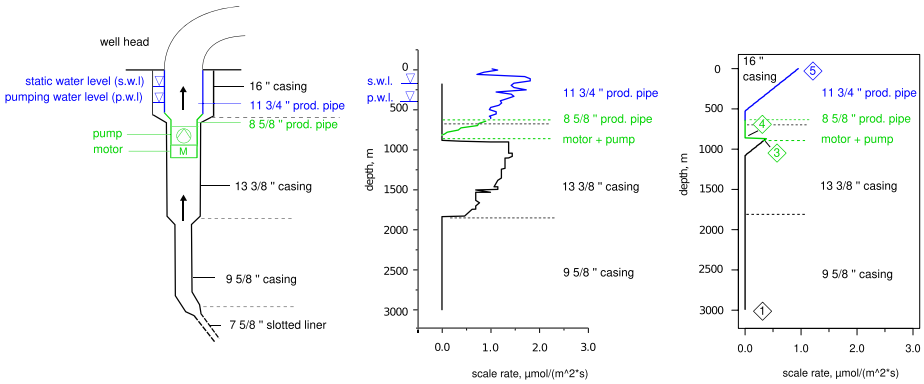

Fig. 9 Left: Schematic drawing of production side at site 6 (not to scale). Middle: Scale rate in the casing (black line) of that site calculated from MFC measurements in 2010 and 2015 with measurements available only below water level. The scale rate in the production pipe (blue and green line) was determined from three time periods. Right: Modeled scale rate based on the regression in Figure 4 b

to an increased $SI_{calcite}$ (Wanner et al. 2017) but still without reaching thermodynamic equilibrium. This effect slows down the scale kinetics. At the same time, however, these gas bubbles gradually redissolve, also kinetically limited. This effect, in contrast to stripping, accelerates scale formation, since stripping keeps on going even if gas bubbles are thermodynamically unstable.

An exponential increase of the scale rate indicates degassing in the pump with only a slow redissolution of gas bubbles towards the wellhead. This exponential shape can slightly be seen at sites 7, 8, and 10 (only red data points). The high degassing pressures of sites 7 and 8 support this.

Where the shape of the curve looks more like a confined exponential growth (site 6), this indicates a fast redissolution of gas bubbles above the ESP.

Even though a kinetic effect of Mg-inhibition on the calcite scale rate at the investigated facilities is likely according to the literature (Gutjahr et al. 1996; Zhang et al. 2001), Mg-inhibition does not clearly show from the observed scale rates, and cannot be quantified from it. For example, facilities 16 and 17 have the same Mg^{2+} concentration but one of it has a lot of scales while the other has no scale at all (see Table 2). This indicates that for modeling of the investigated sites, thermodynamic parameters (here $SI_{calcite}$) are more important than kinetic effects.

Moreover, the shape of scale rate along the pipe is generally also reproducible for each facility, independent of the produced volume. This means that the surface roughness and effective surface area (plain tube wall vs. precipitates on the wall) does not change much over time. This is evident from site 6 where the scale rates during different time periods yielded similar scale rates, although the produced volumes differ by a factor of 3. However, the shape of the scale rate curve is not reproducible if different types of ESP are used or if the operational modes change. Therefore, site 8, which was subject to different ESP types and different operational modes, shows different shapes during different time intervals. A particular feature at site 8 is the increased scale rate closely above the pump which could be caused by the increased degassing from the high number of ESP changes and start cycles. This demonstrates that the kinetics of degassing can be influenced by the operator.

Site 9 shows also a particular feature: this site experimented with coated surfaces (Wanner et al. 2017). The coated pipes scaled slower at the very early stages (Figure 8, black data points) but once a continuous scale layer was attached (blue data points), the scale rate was equal to the uncoated pipes.

In general, looking at all presented measured scale rates (Figure 7, Figure 8), it can be concluded that the thermodynamic drivers Δ p(CO_2), and total pressure work fair for scale prediction. In contrast to that, the kinetic effect of stripping due to the gas load is small. This is evident from the facilities 2, 3a, 3b, and 5 which have no or only little scales despite high gas loadings (Figure 2, 7)

This observation is closely restricted to the applied wellhead pressures. If the wellhead pressures of these facilities were lower, the kinetic effect might become much stronger leading to more scales at these sites. This shows that the thermodynamic scale drivers cannot be avoided by the facility operator but measures can be taken to reduce kinetic effects by increasing the wellhead pressure. Furthermore, reducing the number of pump starts and load changes to a minimum can reduce degassing, CO_2-stripping, and scale kinetics.

Validation of scale rate prediction at the ESP and below

At a last step, we have a closer look at the region around the ESP and motor (Figure 9). This part of the geothermal system (see Figure 1, simulation points 3 and 4) is particularly critical for scale formation since it shows large pressure and temperature changes. Therefore, the prediction of scale rates is extended to this section of the thermal cycle according to the pressure-to-scale rate regression in Figure 4 b).

Figure 9 shows a schematic drawing of the well design (left), together with the real scale rate (middle) calculated from the MFC-inspection, and the modeled scale rate (right) calculated from the regression in Figure 4 b). The real scale rate is zero in the 9 5/8”-diameter pipe. Here the MFC indicated even a diameter increase (corrosion). In the 13 3/8” casing, scale buildup starts and increases towards the ESP. Then due to the higher pressure at the outlet of the pump, the scale rate in the 8 5/8” production casing is lower again. With further decompression in the production pipe (8 5/8 ” and 11 3/4 ”), the scale rate increases again towards the surface. In the 16 ” casing surrounding the production pipe, no scale is observed.

The modeled scale rate below the ESP (9 5/8” and 13 3/8” casing) is qualitatively in accordance with the real scale rate. However, in the model, scale starts at lower depths than observed, and also the modeled scale rates are smaller than predicted. This indicates that already a smaller pressure contrast than expected from the regression in Figure 4 b can lead to scale. In the 16 ” casing surrounding the production pipe, the regression in Figure 4 b can generally not be applied due to the different conditions. Here, the water is not exchanged as in the production pipe so that mass limitation prevents scale buildup.

Regarding the scale drivers in the section below the ESP (9 5/8”, and 13 3/8” casing), the scale in that section is caused by the decreasing partial pressure of CO_2 with decreasing total pressure (Tanger and Helgeson 1988; Shock et al. 1992; Parkhurst and Appelo 2013; Hörbrand et al. 2018). Here, degassing and stripping are not expected since there are no extreme pressure jumps. In contrast to that, in the production pipes (8 5/8 ”, and 11 3/4 ”), also degassing influences the scale rate.

In general, one must keep in mind that the real scale rates in the 9 5/8", 13 3/8", and 16" casing are derived from MFC measurements. This indirect measurement method involves high uncertainties. Therefore, scale rate prediction for this section is less accurate than scale prediction in the production pipes. Therefore, a deviation from of the modeled scale rate from the observed scale rate derived from the MFC is not necessarily wrong but may be an artefact of different measurement approaches.

Conclusion

This study presents a comprehensive dataset of empirical calcite scale rates including 16 sites in the BMB and 1 site in Upper Austria. Scale driving parameters are identified and regressions for the prediction of scale rates are derived. The regressions are validated. In addition, the scale rates are also modeled with existing models (PHREEQC), and the results are compared to the results from the regressions.

The measured scale rates in the production pipes of 13 facilities range from 0 - 1.5 μ mol/($m^2 \cdot s$) above the pump to 1.5 - 4.1 μmol/($m^2 \cdot s$) at the wellhead. The scale rates are too small to allow a prediction of the scale rate based on the change of the hydrochemistry throughout the production pipe.

Also, as seen in our results, the measured scale rate is systematically overestimated by existing hydrogeochemical models (PHREEQC) yielding scale rates which are one order of magnitude too high. One reason for this overestimation are inhibitory effects mainly caused by Mg^{2+}, oil, organic acids, or shear stress. Another reason is that the calcite precipitation kinetics implemented in PHREEQC are based on dissolution experiments, not on precipitation experiments. The backwards reaction, i.e. precipitation may happen more slowly than the dissolution reaction. Furthermore, these models cannot depict the strong increase of the scale rate from the pump to the wellhead, and are hence insufficient. While these models are well suitable for thermodynamic equilibrium calculations, they hence require improvements when used for the calculation of calcite scaling kinetics. This observation is not restricted to the thermal waters from the Bavarian Malm aquifer but is expected to apply also to other geothermal systems with comparable hydrochemistry, pressures, and temperature.

However, scale rates can be predicted by empirical regressions based on thermodynamic parameters by intensive analysis and modeling. Here, based on 6 facilities, the $SI_{calcite}$ is linked to the scale rate by the regression

$f(x) = -4.86 \cdot 10^{-6} + 2.96 \cdot 10^{-5} \cdot x$, where x represents $SI_{calcite}$.

The scale rate can roughly be approximated based on the pressure contrast between the reservoir and the wellhead, already without modeling, with the empirical regression $g(x) = -3.92 \cdot 10^{-6} + 1.96 \cdot 10^{-8} \cdot x$, where x represents pressure. The rationale behind this regression is that temperature changes and temperature effects in the production pipe are much smaller compared to pressure effects. Scale rates calculated with the regressions are validated at seven other facilities and roughly fit most of them.

Deviations from the predicted scale rates are mostly attributed to kinetic effects (CO_2 -stripping, Mg-inhibition, oil, and shear stress on the pipe surfaces due to the fluid flow). Kinetic parameters are hard to study since several parameters change at the same

time. Therefore, until now, they cannot be explicitly implemented in the scale prediction. However, our results show that reasonable scale prediction is already possible based solely on the thermodynamic parameters (Δ log (pCO_2), Δ total pressure, Δ pH, and $SI_{calcite}$) since they are more important than the kinetic effects. Nevertheless, kinetic effects are indirectly incorporated in the presented regressions since the scale rate is a result of thermodynamic and kinetic parameters. Therefore, the order of magnitude of the modeled scale rate is correct, but the kinetic effect cannot be differentiated between the facilities.

The presented regressions for calcite scale prediction are valid for geothermal carbonatic waters with a temperature of 105 - 140 °C, pressure of 5 - 400 bar, and a pH of 6.5 - 6.8. A pH of 6.2 - 7.0 is possibly still acceptable. The indicated pH refers to the modeled conditions inside the pipes and not to the pH measured during water sample collection after cooling and at atmospheric pressure. Proper scale rate prediction is reached for the production pipe, while the regressions underestimate the scale rate below the ESP. The regressions can be transferred with caution to geothermal waters from other carbonatic aquifers as long as the temperature, pressure, and pH are within the range of validity. Major differences in the other hydrochemical parameters may also lead to a derivation from the regressions.

Future research should aim for the extension of the empirical data set to refine the regressions presented in our study. A larger data set consisting of multiple scale measurements at different sites, together with an implementation of a hydrodynamic model could allow to explicitly include kinetic parameters in the prediction of scale rates. This might require the installation of additional sensors in the production pipe. Furthermore, an interesting research aspect is the kinetic effect of oil and shear forces at the fluid–crystal interface on the scale rate.

In the wider technical and economical context, the acquired improved process understanding and the quantitative scale prediction are expected to be very useful. Our manuscript may help the operators to identify the critical points and develop targeted counter measures. Possible counter measures include addition of chemical inhibitors such as polycarboxylates which need to be biodegradable according to the regional regulations of the Bayerisches Landesamt für Umwelt. The addition of CO_2 to the produced fluid represents another option to reduce carbonate scale. The scale distributions presented in this manuscript show the need of application of these inhibitory measures already below the ESP. Where no counter measures are available, scale prediction helps the planning of maintenance intervals and the risk assessment of technical failures already based on the hydrochemical conditions and on the operational parameters.

Supplementary information

Supplementary information accompanies this paper at https://doi.org/10.1186/s40517-020-00180-x .

Additional file 1. Kinetics of calcite dissolution according to Plummer (1978) as implemented in PHREEQC

Additional file 2. Plot calculated with PHREEQC showing that for a selected geothermal facility, the pressure drop from the reservoir to the wellhead leads to an SI of 0.20 at the wellhead. The plot also shows that the correlation is almost linear.

Additional file 3. Plot calculated with PHREEQC showing that the temperature reduction in the production pipe has a smaller effect on the SI than the pressure drop. Typical temperature loss in the production pipe is 1-2 K, and even a temperature change of 6 K changes the SI only for about 0.10 SI units.

Abbreviations
BMB: Bavarian Molasse basin; ESP: Electrical submersible pump; MFC: Multifinger caliper measurement; $p(CO_2)$: partial pressure of CO_2; SEM-EDX: Scanning electron microscope with energy-dispersive X-ray spectroscopy; SI: Saturation index; $SI_{calcite}$: Saturation index of calcite; XRD: X-ray diffraction.

Acknowledgements
The financial support by the Bayerisches Staatsministerium für Wissenschaft und Kunst is gratefully acknowledged. We thank the Stadtwerke München for providing us the access to their geothermal facilities, to their scanning electron microscope and laboratory and for supplying us with the operational data. We also thank all other operators of geothermal facilities for giving us access to their facilities and operational data. We would very much like to thank Dr. Martina Ueckert for multiple readings and discussions of the manuscript. Furthermore, we thank Christine Benning for SEM-EDX measurements and acid digestions, Andrea Abram for the Raman micro-spectroscopy measurements, and Amanada Günther for the XRD measurements.

Authors' contributions
BK did the field work, scale analyses, scale rate evaluation, hydrogeochemical modeling, and graphical representations. TB initiated the project, developed the hydrogeochemical modeling framework, discussed the results with BK, and refined the evaluation and hydrogeochemical model. ME discussed the results with BK and TB, structured, and supported the evaluation. All authors read and approved the final manuscript.

Funding
Open Access funding enabled and organized by Projekt DEAL. This work was partially funded by the Bavarian Ministry of Science and Art in the project Geothermie-Allianz Bayern.

Availability of data and materials
The datasets used and analyzed during the current study are available from the corresponding author on reasonable request.

Competing interests
The authors declare that they have no competing interests.

Author details
[1] Chair of Analytical Chemistry and Water Chemistry, Technical University of Munich, Marchioninistrasse 17, 81377 München, Germany. [2] Chair of Hydrogeology, Technical University of Munich, Arcisstr. 21, 80333 München, Germany.

Received: 7 July 2020 Accepted: 8 September 2020
Published online: 20 October 2020

References

Andritsos N, Karabelas AJ, Koutsoukos PG. Morphology and structure of caco3 scale layers formed under isothermal flow conditions. Langmuir **13**, 2873–2879
Appelo CAJ, Postma D. Geochemistry, Groundwater and Pollution. A.A. Balkema Publishers
Leygraf C, Odnevall Wallinder I, Tidblad J, Graedel T. Atmospheric gases and their involvement in corrosion, pp. 34–45. John Wiley & Sons, Ltd (2016). Chap. 4. https://doi.org/10.1002/9781118762134.ch4.
Avramov I. Relationship between diffusion, self-diffusion and viscosity. Journal Non-Crystalline Solids. 2009;355(10):745–7. https://doi.org/10.1016/j.jnoncrysol.2009.02.009 Glass and Entropy.
Bauer M, Freeden W, Jacobi H, Neu T. Handuch Tiefe Geothermie. Berlin Heidelberg: Springer; 2014.
Baumann T. Validation of hydrochemical analyses and gas concentrations of deep geothermal aquifers. In: 41st Workshop on Geothermal Reservoir Engineering, pp. 1269–1277. Stanford University, Stanford 2016. https://pangea.stanford.edu/ERE/pdf/IGAstandard/SGW/2016/Baumann.pdf
Bayerisches Staatsministerium: Energie Atlas Bayern. last accessed 22.5.2019; 2019. https://www.energieatlas.bayern.de/thema_geothermie/tiefe/daten.html
Beck R, Andreassen J-P. Influence of crystallization conditions on crystal morphology and size of caco3 and their effect on pressure filtration. AIChE Journal. 2012;58(1):107–21. https://doi.org/10.1002/aic.12566.
Boch R, Leis A, Haslinger E, Goldbrunner J, Mittermayr F, Froeschl H, Hippler D, Dietzel M. Scale-fragment formation impairing geothermal energy production: interacting h2s corrosion and caco3 crystal growth: interacting h2s corrosion and caco3 crystal growth. Geothermal Energy. 2017;5:1–19. https://doi.org/10.1186/s40517-017-0062-3.
Chou L, Garrels RM, Wollast R. Comparative study of the kinetics and mechanisms of dissolution of carbonate minerals. Chemical Geology. 1989;78(3):269–82. https://doi.org/10.1016/0009-2541(89)90063-6 Kinetic Geochemistry.
Dreybrodt W, Buhmann D, Michaelis J, Usdowski E. Geochemically controlled calcite precipitation by co2 outgassing: Field measurements of precipitation rates in comparison to theoretical predictions. Chemical Geology. 1992;97(3):285–94. https://doi.org/10.1016/0009-2541(92)90082-G.
Eichinger F. Anwendung von verschiedenen Inhibitoren zur Vermeidung von Ausfällungen und Korrosion in Tiefengrundwassersystemen im Molassebecken und Norddeutschen Becken - Thermoinhibitor. Hydroisotop: Technical report; 2016.
Eyerer S, Schifflechner C, Hofbauer S, Wieland C, Zosseder K, Bauer W, Baumann T, Heberle F, Hackl C, Irl M, Spliethoff H. Potential der hydrothermalen Geothermie zur Stromerzeugung in Deutschland. Technical report, Lehrstuhl für Energiesysteme, Technische Universität München 2017.

Flechtner F, Aubele K. A brief stock take of the deep geothermal projects in bavaria. In: Proceedings, 44th Workshop on Geothermal Reservoir Engineering, Stanford, California 2019. Stanford University
Furtak H, Langguth H-R. Zur hydrochemischen Kennzeichnung von Grundwässern und Grundwassertypen mittels Kennzahlen. IAH-Congress. 1965;7:89–96.
Ganor J, Lasaga A. Simple mechanistic models for inhibition of a dissolution reaction. Geochimica et Cosmochimica Acta. 1998;62:1295–306. https://doi.org/10.1016/S0016-7037(98)00036-2.
Gutjahr A, Dabringhaus H, Lacmann R. Studies of the growth and dissolution kinetics of the caco 3 polymorphs calcite and aragonite ii. the influence of divalent cation additives on the growth and dissolution rates. Journal of Crystal Growth. 1996;158:310–5.
Herbrich M. Anlagen- und sicherheitsrelevante Prozesse im Thermalwasserkreislauf eines geothermischen Heizkraftwerks. PhD thesis, Technische Universität München. http://nbn-resolving.de/urn/resolver.pl?urn:nbn:de:bvb:91-diss-20161209-1310243-0-3
Herbrich M, Nießner R, Baumann T. Minimierung von Risiken bei Planung und langfristigem Betrieb tiefengeothermischer Anlagen im bayerischen Molassebecken.- Schlussbericht. Forschungsbericht, Institut für Wasserchemie, Technische Universität München 2015. Förderkennzeichen: 0325280B. https://doi.org/10.2314/GBV:84078233010.2314
Herman JS, Lorah MM. Calcite precipitation rates in the field: Measurement and prediction for a travertine-depositing stream. Geochimica et Cosmochimica Acta. 1988;52(10):2347–55. https://doi.org/10.1016/0016-7037(88)90292-X.
Hörbrand T, Baumann T, Moog HC. Validation of hydrogeochemical databases for problems in deep geothermal energy. Geothermal Energy. 2018;6(20):
Huang F, Liang Y, He Y. On the pickering emulsions stabilized by calcium carbonate particles with various morphologies. Colloids Surfaces A Physicochemical and Engineering Aspects. 2019;580:123722. https://doi.org/10.1016/j.colsurfa.2019.123722.
Tanger JC, Helgeson HC. Calculation of the thermodynamic and transport properties of aqueous species at high pressures and temperatures; revised equations of state for the standard partial molal properties of ions and electrolytes. Am J Sci. 1988;288(1):19–98.
Kahyarian A, Achour M, Nesic S. 7 - co2 corrosion of mild steel. In: El-Sherik, A.M. (ed.) Trends in Oil and Gas Corrosion Research and Technologies. Woodhead Publishing Series in Energy, pp. 149–190. Woodhead Publishing, Boston 2017. https://doi.org/10.1016/B978-0-08-101105-8.00007-3. http://www.sciencedirect.com/science/article/pii/B9780081011058000073
Karabelas AJ. Scale formation in tubular heat exchangers-research priorities. Int. J. Therm. Sci. 2002;41:682–92.
Langmuir D. The geochemistry of some carbonate ground waters in central pennsylvania. Geochimica et Cosmochimica Acta. 1971;35:1023–45. https://doi.org/10.1016/0016-7037(71)90019-6.
Larsen PA, Patience DB, Rawlings JB. Industrial crystallization process control. IEEE Control Sys Magazine. 2006;26(4):70–80. https://doi.org/10.1109/MCS.2006.1657878.
Latosov E, Loorits M, Maaten B, Volkova A, Soosaar S. Corrosive effects of h2s and nh3 on natural gas piping systems manufactured of carbon steel. Energy Procedia. 2017;128:316–23. https://doi.org/10.1016/j.egypro.2017.08.319.
Mayrhofer C. Hydrochemische Untersuchungen im Malmaquifer im bayerischen Molassebecken. Dissertation, Technische Universität München, München 2013. https://mediatum.ub.tum.de/?id=1128419
Merkel B, Arab A. Verhinderung von Calcit Ausfällungen in der Tiefen Geothermie. In: Der Geothermiekongress 2018, Essen
Parkhurst DL, Appelo CAJ. Description of input and examples for PHREEQC version 3 – a computer program for speciation, batch-reaction, one-dimensional transport, and inverse geochemical calculations. Technical Report Techniques and Methods 6–A43, U.S. Geological Survey 2013. http://pubs.usgs.gov/tm/06/a43/
Parkhurst DL, Appelo CAJ. User's guide to phreeqc (version 2)–a computer program for speciation, batch-reaction, one-dimensional transport, and inverse geochemical calculations. Technical report, U.S. Geological Survey 1999. https://doi.org/10.3133/wri994259
Plummer LN, Wigley TML, Parkhurst DL. The kinetics of calcite dissolution in CO_2-water systems at 5° to 60 ° C and 0.0 to 1.0 Atm CO2. American Journal of Science 1978;278, 179–216.
Plummer LN, Busenberg E, Riggs AC. In-situ growth of calcite at devils hole, nevada: Comparison of field and laboratory rates to a 500,000 year record of near-equilibrium calcite growth. Aquatic Geochemistry. 2000;6(2):257–74. https://doi.org/10.1023/A:1009627710476.
Popoola LT, Grema AS, Latinwo G, Gutti B, Balogun A. Corrosion problems during oil and gas production and its mitigation. International Journal of Industrial Chemistry. 2013;4: https://doi.org/10.1186/2228-5547-4-35.
Richard D, Speck T. The role of shear in crystallization kinetics: From suppression to enhancement. Scientific Reports. 2015;5: https://doi.org/10.1038/srep14610.
Sanjuan B, GirardJP. Review of kinetic data on carbonate mineral precipitation, brgm report r39062. Technical report 1996
Schindelin J, Arganda-Carreras I, Frise E, Kaynig V, Longair M, Pietzsch T, Preibisch S, Rueden C, Saalfeld S, Tinevez J-Y, White DJ, Hartenstein V, Eliceiri K, Tomancak P, Cardona A. Fiji: an open-source platform for biological-image analysis. Nature Methods 2012;676(9). https://doi.org/10.1038/nmeth.2019
Schröder H, Hesshaus A. Langfristige Betriebssicherheit geothermischer Anlagen. Bundesanstalt für Geowissenschaften und Rohstoffe (BGR), Hannover: Technical report; 2009.
Shock EL, Oelkers EH, Johnson JW, Sverjensky DA, Helgeson HC. Calculation of the thermodynamic properties of aqueous species at high pressures and temperatures. effective electrostatic radii, dissociation constants and standard partial molal properties to 1000° c and 5 kbar. J. Chem. Soc., Faraday Trans. 1992;88, 803–826. https://doi.org/10.1039/FT9928800803
Stadtwerke München: SWM Fernwärme-Vision. last accessed 22.5.2019; 2019. https://www.swm.de/privatkunden/unternehmen/energie/vision-fernwarme.html
Svensson U, Wolfgang D. Dissolution kinetics of natural calcite minerals in co2-water systems approaching calcite equilibrium. Chemical Geol. 1992;100(1–2):129–45. https://doi.org/10.1016/0009-2541(92)90106-F.
Talman SH, Wiwchar B, Gunter WD, Scarfe CM. Dissolution kinetics of calcite in the $H_2O - CO_2$ system along the steam saturation curve to 210 ° C. The Geochemical Society 1990.

Tegethoff WF (ed.): Calciumcarbonat. Von der Kreidezeit Ins 21. Jahrhundert. Springer, Basel, Boston, Berlin 2013.
Wanner C, Eichinger F, Jahrfeld T, Diamond LW. Causes of abundant calcite scaling in geothermal wells in the Bavarian Molasse Basin, Southern Germany. Geothermics. 2017;70:324–38. https://doi.org/10.1016/j.geothermics.2017.05.001.
Zaihua L, Svensson U, Dreybrodt W, Daoxian Y, Buhmann D. Hydrodynamic control of inorganic calcite precipitation in huanglong ravine, china: Field measurements and theoretical prediction of deposition rates. Geochimica et Cosmochimica Acta. 1995;59(15):3087–97. https://doi.org/10.1016/0016-7037(95)00198.
Zhang Y, Shaw H, Farquhar R, Dawe R. The kinetics of carbonate scaling- application for the prediction of downhole carbonate scaling. Journal of Petroleum and Engineering. 2001;29:85–95.
Zhao X, Chen XD. A critical review of basic crystallography to salt crystallization fouling in heat exchangers. Heat Transfer Engineering. 2013;34(8–9):719–32. https://doi.org/10.1080/01457632.2012.739482.

Publisher's Note